94-GHz Imager With Extended Depth of Field

Joseph N. Mait, *Senior Member, IEEE*, David A. Wikner, Mark S. Mirotznik, *Member, IEEE*,
Joseph van der Gracht, Gregory P. Behrmann, Brandon L. Good, and Scott A. Mathews, *Member, IEEE*

***Abstract*—We describe a computational imaging technique to extend the depth-of-field of a 94-GHz imaging system. The technique uses a cubic phase element in the pupil plane of the system to render system operation relatively insensitive to object distance. However, the cubic phase element also introduces aberrations but, since these are fixed and known, we remove them using post-detection signal processing. We present experimental results that validate system performance and indicate a greater than four-fold increase in depth-of-field from 17” to greater than 68”.**

***Index Terms*—Computational imaging, extended depth of field, millimeter wave imaging.**

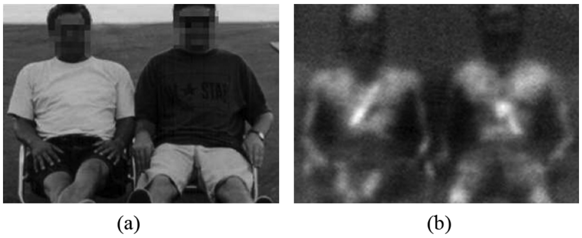
(a) (b)

Fig. 1. Gigahertz imaging through clothing. (a) Visible image of scene. (b) 94-GHz image of weapons concealed under clothing.

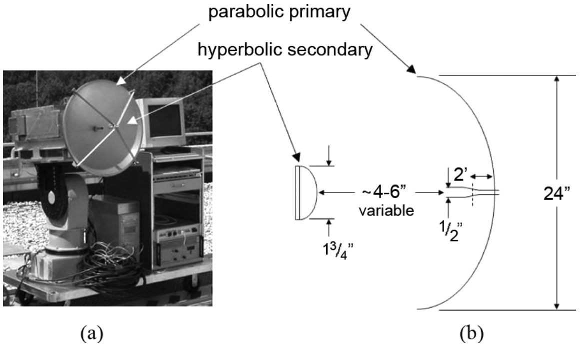

Fig. 2. 94-GHz scanning imaging system. (a) Image of system. (b) Schematic representation with measured dimensions.

I. Introduction

The ability of gigahertz and terahertz frequencies to penetrate materials that are impenetrable at optical frequencies has prompted recent interest in the development of millimeter wave sources and detectors [1]. Applications of this capability include, for example, the detection of concealed weapons under clothing [2], [3]. However, unlike the stationary figures shown in Fig. 1, a more typical scenario for this application is screening individuals at points of ingress, such as the entrance to a building or the secured portion of an airport. To enhance the performance of screening systems, one would prefer to observe individuals as long as possible as they pass through a volume. This improves the chances of detecting a hidden object. (It might also reduce bottlenecks created at portals.) However, wavelength and system considerations limit focused imaging to only a narrow volume in depth, or depth-of-field. Thus, a screener has only a short amount of time to detect the presence or absence of a concealed weapon. Extending the depth-of-field provides the screener with more time to observe an individual.

A similar problem occurs in iris recognition for security applications, for example, logging-on to a computer system. In this situation the narrow depth of field produces unnatural head movements as a user seeks to place his or her iris in the object plane of the optical system. Extending the depth-of-field for these systems has been addressed using computational imaging techniques [4]–[7]. By computational imaging, we mean an imaging system whose pre-detection optics and post-detection signal processing are designed jointly to achieve a result that is not possible using only optics or only signal processing [8], [9]. For example, placing an optical element with cubic-phase in the pupil plane of the optical system renders system operation relatively insensitive to object distance. However, the cubic phase also generates an aberrated image. But, since the aberrations are known, one can correct them using simple post-detection signal processing. Since the system response is effectively invariant to object location, the combination of optical and electronic processing yields a system with larger depth-of-field than a conventional system.

In this work we describe our application of this technique for extended depth-of-field imaging to a 94-GHz system and present experimental results to verify its performance. In Section II we describe our imaging system and present a mathematical description of its operation with and without extended depth-of-field. We describe design and fabrication of the cubic-phase element in Section III and present experimental results in Section IV. Section V discusses the signal processing required by the cubic phase system to realize the extended depth and presents the results from this processing. We end in Section VI with summary remarks on our approach.

II. 94-GHz Imaging System

Our imaging system, represented in Fig. 2, is a 94-GHz Stokes-vector radiometer used for millimeter wave phenomenology measurements [10]. It is a single-beam system

---

Manuscript received December 18, 2007; revised June 04, 2008. Current version published June 03, 2009.

J. N. Mait and D. A. Wikner are with the U.S. Army Research Laboratory, Adelphi, MD 20783 USA (e-mail: jmait@arl.army.mil).

M. S. Mirotznik, G. P. Behrmann, B. L. Good, and S. A. Mathews are with the Department of Electrical Engineering, Catholic University of America, Washington, DC 20064 USA.

J. van der Gracht is with Holospex, Columbia, MD 21044 USA.

Digital Object Identifier 10.1109/TAP.2009.2019882

that forms an image by scanning in azimuth and elevation. The radiometer has a thermal sensitivity of 0.3 K with a 30-ms integration time and 1-GHz bandwidth per pixel. A Cassegrain antenna is mounted to the front of the radiometer receiver. It has a 24”-diameter primary parabolic reflector and a 1.75”-diameter secondary hyperbolic reflector. The position of the hyperbolic secondary is variable.

If we model the 94-GHz imager as a linear, spatially incoherent, quasi-monochromatic system, the intensity of the detected image can be represented as a convolution between the intensity of the image predicted by geometrical optics with the system point spread function [11]

$$|i(x,y)|^2 = o_g(x,y) ** h(x,y) \tag{1}$$

where $**$ represents a two-dimensional convolution. The function $o_g(x,y)$ represents the inverted, magnified image of the object that a ray-optics analysis of the system predicts

$$o_g(x,y) = \frac{1}{M^2}\left|o\left(\frac{-x}{M}, \frac{-y}{M}\right)\right|^2. \tag{2}$$

If the object and image distances are d_o and d_i, respectively, the magnification M is

$$M = \frac{d_i}{d_o}. \tag{3}$$

For the purposes of geometrical analysis, we can model the system as a single lens imaging system with $d_i = 6''$ (152.4 mm)

$$\frac{1}{d_o} + \frac{1}{d_i} = \frac{1}{f}. \tag{4}$$

The value of d_i is based on measurements of the antenna. We adjusted the position of hyperbolic element so that nominal operation of the imager is with $d_o = 180''$ (4572 mm). Thus, the effective focal length of the system is $f = 5.81''$ (147.6 mm).

The second term in (1), $h(x,y)$, is the incoherent point spread function (PSF). It accounts for wave propagation through the aperture

$$h(x,y) = \frac{1}{(\lambda f)^4}\left|p\left(\frac{-x}{\lambda f}, \frac{-y}{\lambda f}\right)\right|^2 \tag{5}$$

where $p(x/\lambda f, y/\lambda f)$ is the coherent point spread function. The function $p(x,y)$ is the inverse Fourier transform of the system pupil function $P(u,v)$

$$p(x,y) = \mathrm{FT}^{-1}\left[P(u,v)\right]. \tag{6}$$

As a consequence, the optical transfer function (OTF) $H(u,v)$ associated with the PSF is the autocorrelation of the pupil function $P(u,v)$ with frequency axes scaled by λf

$$H(u,v) = P(\lambda f u, \lambda f v) \star\star P(\lambda f u, \lambda f v) \tag{7}$$

where $\star\star$ represents two-dimensional correlation. For example, for a circular aperture of diameter D

$$P(u,v) = \mathrm{circ}\left(\frac{2\sqrt{u^2+v^2}}{D}\right) \tag{8}$$

the PSF $h(x,y)$ is, to within a constant

$$h(x,y) = \frac{\pi^2}{4}\left(\frac{D}{\lambda f}\right)^4 \left[\frac{J_1\left(\frac{\pi D\sqrt{x^2+y^2}}{\lambda f}\right)}{\frac{\pi D\sqrt{x^2+y^2}}{\lambda f}}\right]^2. \tag{9}$$

Ray analysis of our system confirmed that the parabolic primary forms the aperture stop, i.e., it defines the location of the pupil plane.

Displacement d_ϵ of an object from the nominal object plane introduces a phase error $\theta_\epsilon(u,v)$ in the pupil function [11]

$$P_\epsilon(u,v) = \exp\left[-j\theta_\epsilon(u,v)\right]\mathrm{circ}\left(\frac{2\sqrt{u^2+v^2}}{D}\right) \tag{10}$$

where

$$\theta_\epsilon(u,v) = \left(\frac{\pi}{\lambda}\right)\left(u^2+v^2\right)\left(\frac{1}{d_o+d_\epsilon} - \frac{1}{d_o}\right). \tag{11}$$

The phase error increases the width of a point response. If the displacement and phase errors are small, the detector (either human or machine) may be unable to resolve the increase and the image is perceived as in-focus.

The distance in object space over which an object can be placed and still produce an in-focus image is the system's depth-of-field DoF

$$DoF = d_{o+} - d_{o-} \tag{12}$$

where formulas for d_{o+} and d_{o-} depend upon system application. Many different definitions exist. For demonstration purposes, we use a conventional definition based on the spatial extent δ of the point response [12]

$$d_{o+} = \frac{d_i}{\left(\frac{d_i}{f-1}\right) - \frac{\delta}{D}} \tag{13}$$

and

$$d_{o-} = \frac{d_i}{\left(\frac{d_i}{f-1}\right) + \frac{\delta}{D}}. \tag{14}$$

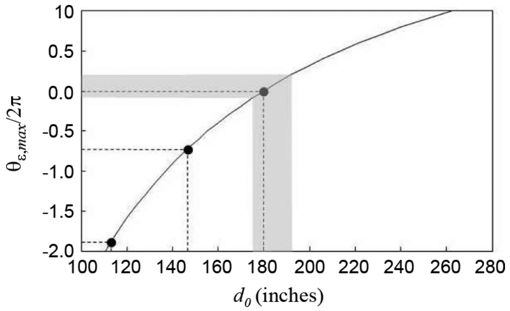

Fig. 3. Maximum relative pupil phase error as a function of object distance. The shaded region indicates a conventional depth of field. The discrete points indicate object distances used in experiments.

Under the assumptions that δ is defined by the Rayleigh criteria, the imager operates in the far-field $(d_o \gg f)$, and the lens aperture is large compared to a wavelength

$$DoF \approx (2.44\lambda)\left(\frac{d_o}{D}\right)^2. \tag{15}$$

For a 94 GHz-imager with $D = 24''$ and $d_o = 180''$, $DoF \approx 17.4''$ which ranges from 175.2" to 192.6". Fig. 3 indicates the maximum relative phase error as a function of object distance and also indicates the region we have defined as being in the depth-of-field. (The maximum error for a given plane occurs at the edge of the aperture, $u^2 + v^2 = D^2/4$.)

Equation (15) explains mathematically what any good photographer already knows: one can increase DoF by decreasing ("stopping down") the lens aperture D. However, this reduces throughput and degrades the diffraction limited resolution. Alternatively, it has been shown at optical wavelengths that a cubic-phase element placed in the pupil plane of an imaging system in combination with post-detection processing can also increase DoF but without sacrificing either throughput or resolution.

The cubic phase element $P_c(u, v)$ is

$$P_c(u, v) = \exp\left[j\theta_c(u, v)\right] \operatorname{rect}\left(\frac{u}{W_u}, \frac{v}{W_v}\right) \tag{16}$$

where

$$\theta_c(u, v) = (\pi\alpha)\left[\left(\frac{2u}{W_u}\right)^3 + \left(\frac{2v}{W_v}\right)^3\right]. \tag{17}$$

The phase function is separable in the u- and v-spatial frequencies and has spatial extent W_u and W_v along the respective axes. The constant α represents the strength of the cubic phase. Along one axis the total phase change is $2\pi\alpha$; the phase change across a diagonal is $4\pi\alpha$. In the simulations presented below, we modified the model for $P_c(u, v)$ slightly and included an appropriately sized central obscuration to account for the effect of rays blocked by the secondary mirror.

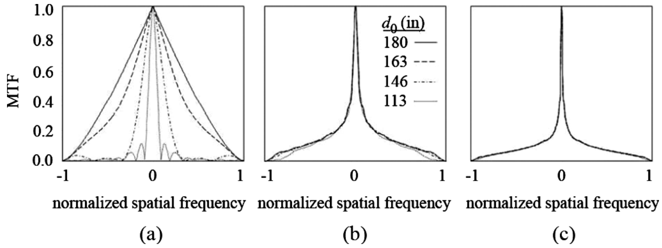

Fig. 4. Modulation transfer function for systems with different strength cubic phase: (a) $\alpha = 0$, (b) $\alpha = 7$, and (c) $\alpha = 20$. The MTFs for four different object distances are represented: 180" (solid line), 163" (dashed line), 146.5" (dot-dashed line), and 113" (dotted line).

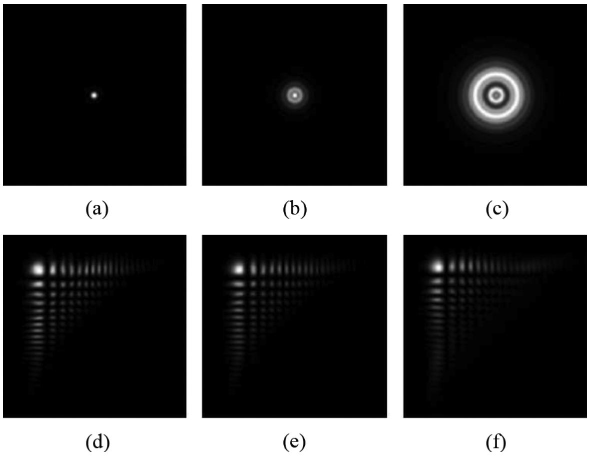

Fig. 5. Simulated point spread functions for conventional imaging and imaging with a cubic phase. Simulated PSFs for conventional imaging system at (a) 180", (b) 146.5", and (c) 113". (d)-(f) Simulated PSFs for an imaging system with cubic phase at the same object distances as (a)-(c).

Representations of the magnitude transfer function (MTF), the magnitude of the OTF $|H(u, v)|$, in cross-section are represented in Fig. 4 for three different values of $\alpha = \{0, 7, 20\}$ and different values of misfocus. (The misfocused planes are located roughly at 1, 2, and 4 times the DoF. The values noted in the figure are measured distances used in our experiments.) A conventional system with no cubic phase ($\alpha = 0$) is represented in Fig. 4(a). Note that the MTFs differ for each value of misfocus. Compensating for misfocus therefore requires *a priori* knowledge of where an object is located. Even if this information were known, due to the presence of zeros in the MTFs, inverting any one of them is ill-posed and will generate noisy results.

In contrast, the MTFs for cubic phase elements with non-zero values of α are relatively constant over an extended range. Note that the larger the value of α the larger the range over which the system is insensitive to object location. However, increasing α reduces the magnitude of the MTF, which is detrimental for applications with low signal to noise ratios. But, because the MTFs do not contain any zeros, their inversion is better conditioned than the MTFs for a conventional system.

Simulations of the point spread functions one can expect from our imaging system with and without a cubic phase element with $\alpha = 7$ are represented in Fig. 5. The response of the cubic phase system is relatively unchanged, whereas the response of the conventional system changes considerably. We address in

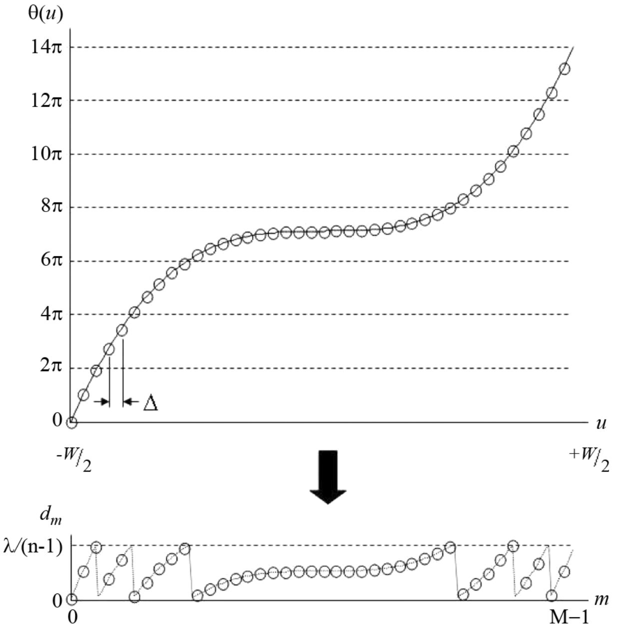

Fig. 6. Representation of the process for converting the cubic phase to a surface depth profile. Only a one-dimensional representation is shown but extensions to two-dimensions are straightforward.

Section V the processing required by the cubic phase system to produce a well-defined spot.

III. Cubic Phase Design and Fabrication

We fabricated a cubic phase element with $\alpha = 7$ from Rexolite using a 3-axis computerized numerical control router. The router has a 0.1969”-minimum feature size (5 mm) and provides 0.0002” $(5\ \mu\mathrm{m})$ position accuracy. Element fabrication was a two-step process.

In the first step we machined a continuous surface profile by sampling the cubic phase $\theta_c(u,v)$, converting phase to depth, and using a cubic spline to insure a smooth transition between depth samples. The phase samples were generated according to

$$\theta_{\ell m} = \sum_{\ell=0}^{L-1} \sum_{m=0}^{M-1} \theta_c \left(u - \frac{W_u}{2}, v - \frac{W_v}{2}\right) \delta \left(u - \frac{m}{\Delta}, v - \frac{\ell}{\Delta}\right). \tag{18}$$

We used a sampling distance $\Delta = 0.1''$ (2.54 mm) to insure overlapping features. Given $W_u = W_v = 24''$, $L = M = 240$.

Phase values were converted to depth $d_{\ell m}$ using

$$d_{\ell m} = \left[\frac{\lambda}{2\pi(n-1)}\right] \left[\theta_{\ell m} \text{ modulo } 2\pi\right]. \tag{19}$$

The modulo-2π operator limits the phase to only a single wavelength and reduces element weight. See Fig. 6. The diffractive characteristics introduced in this conversion have little effect on the response of the element [5], [6]. At 94 GHz Rexolite has a refractive index $n = 1.59$; thus, a depth change of 0.2129” (5.4 mm) in the material generates a 2π-phase change in the wavefront. The second step sharpened the edges at phase discontinuities to within < 0.1 mm. The final element is shown in Fig. 7 mounted to the antenna.

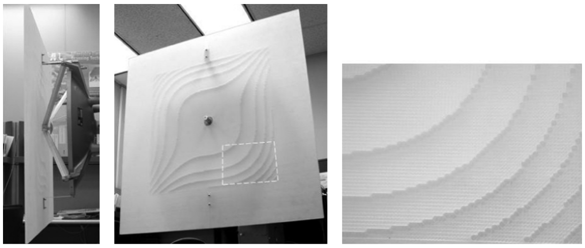

(a) (b) (c)

Fig. 7. Fabricated cubic phase element. (a) Side-view and (b) front-view of cubic phase element mounted to imaging system. (c) Detail of fabricated element. The region displayed is in the lower right of the phase element, which is highlighted in (b).

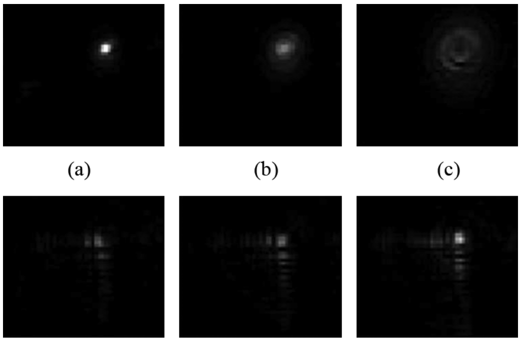

(d) (e) (f)

Fig. 8. Measured point spread functions for conventional imaging and imaging with a cubic phase. PSFs for conventional imaging system at (a) 180”, (b) 146.5” and (c) 113”. (d)-(f) PSFs for a system with cubic phase at the same object distances for (a)-(c).

IV. Experimental Results

To validate the performance of the cubic phase element to extend DoF, we measured the PSF of a conventional system and the cubic-based system at three distances, 113” (2870 mm), 146.5” (3721 m), and 180” (4572 mm). Since the DoF is asymmetric with respect to the object plane and collapses more quickly as the object plane moves toward the system, we measured only this behavior. The out-of-focus object planes correspond to displacements that are twice and four times the calculated DoF. We also imaged an extended object at the same distances using both systems.

To measure the PSF we imaged a point source generated by an open waveguide with dimensions 0.050” × 0.100”. Given that the operating frequency was 94 GHz, the aperture in wavelengths is $0.40\lambda \times 0.80\lambda$. The output power was -14 dBm. The results are represented in Fig. 8. The experimental results agree qualitatively with the simulations presented in Fig. 5. The figures are normalized to the peak value measured, which occurs in Fig. 8(a).

The extended object used in our experiments is represented in Fig. 9(a). The spoke pattern produces 50–50 square waves whose frequencies vary linearly from low values at the circumference to high values in its center. Given that the pattern con-

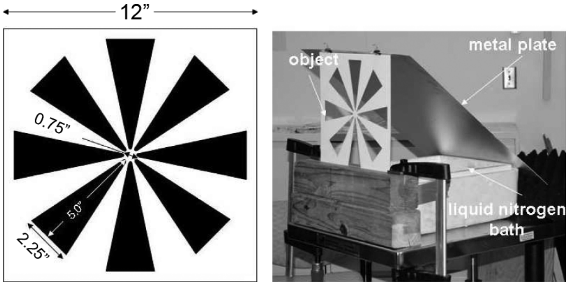

(a) (b)

Fig. 9. (a) Representation of the extended object used to compare conventional and cubic-phase imaging. (b) Schematic of object illumination.

TABLE I
PARAMETERS FOR EXTENDED OBJECT IMAGING

d_o (inches)	M	ρ_{min}	ρ_{max}	r_c/r_{max}
180.0	0.0334	9.7127	139.4409	0.5909
146.5	0.0413	7.8448	112.6238	0.4772
113.0	0.0542	5.9768	85.8067	0.3636

tains 8 periods within one rotation, the period S of the imaged square wave as a function of radius r is

$$S = \frac{2\pi r M}{8} \tag{20}$$

and the corresponding spatial frequency ρ is

$$\rho = \frac{1}{S\lambda f}. \tag{21}$$

The maximum radius $r_{\max} = 5.38''$ and the minimum $r_{\min} = 0.38''$. Since the cutoff frequency for a circular aperture ρ_c is

$$\rho_c = \frac{D}{2\lambda f} \tag{22}$$

the corresponding radius r_c is determined by equating (21) and (22)

$$r_c = \frac{8}{D\pi M}. \tag{23}$$

Radii within the range $r_{\max} \geq r \geq r_c$ generate frequencies in the passband of the optical system. Higher frequencies contained in the region $r_c \geq r \geq r_{\min}$ are cutoff. Table I lists the magnification, minimum and maximum spatial frequencies, and the cutoff radius as a fraction of the maximum radius for the three object distances used in the experiments. We note that beyond 304" the system is incapable of resolving the target at all.

The extended object was generated by placing a metal plate cut-out of Fig. 9(a) in front of a metal reflector angled at 45° to a bath of liquid nitrogen. See Fig. 9(b). This arrangement produces a contrast between the surrounding metal reflecting ambient room temperature and the temperature of the liquid nitrogen reflected through the cut-out. The images captured by the system are represented in Fig. 10.

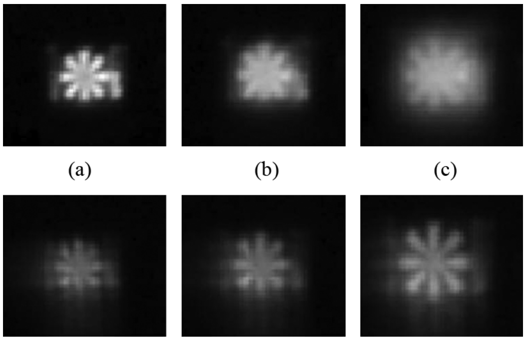

(a) (b) (c)

(d) (e) (f)

Fig. 10. Images of an extended object for conventional imaging and imaging with a cubic phase. Images from a conventional imaging system at (a) 180", (b) 146.5" and (c) 113". (d)-(f) Images from a system with cubic phase at the same object distances for (a)-(c).

Note that the MTF of the conventional system produces images with significant high frequency loss. In contrast, the entire band of frequencies between $\rho_{\min}$ and ρ_c can be seen in the images captured using a cubic phase element. Even without signal processing these images retain more discernable characteristics of the spoke target than the image from the conventional system.

V. POST-DETECTION SIGNAL PROCESSING AND RESULTS

Removing the artifacts of the aberrations introduced by the cubic phase element requires post-detection electronic processing. We assumed a linear process

$$i_p(x,y) = |i\,(x,y)|^2 ** w(x,y) \tag{24}$$

and implemented $w(x,y)$ as a Wiener filter in Fourier space

$$W(u,v) = \frac{H_c^*(u,v)}{|H_c(u,v)|^2 + \frac{K^{-2}\hat{\Phi}_N(u,v)}{\hat{\Phi}_L(u,v)}}. \tag{25}$$

The optical transfer function (OTF) $H_c(u,v)$ associated with the cubic phase element was estimated from the experimentally measured point response images. The parameter K is a measure of the signal-to-noise ratio. The functions $\hat{\Phi}_L(u,v)$ and $\hat{\Phi}_N(u,v)$ are the expected power spectra of the object and noise, respectively. Research has shown that Wiener power spectra are good assumptions for natural scenes [13]. We adjusted the mean spatial detail parameter to produce restored PSFs with widths comparable to that of the experimentally measured focused point. Further, we assumed a flat noise spectrum with $K = 50$.

Reconstructed PSFs are represented in Fig. 11. In Fig. 11(a)–(c), the cubic OTF was estimated from the PSF measured experimentally at 146.5" and the subsequent reconstruction filter applied to all the images. In Fig. 11(d)–(f),

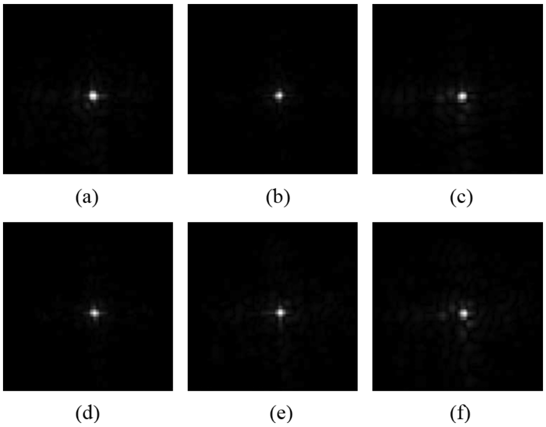

Fig. 11. Processed point responses from a system with cubic phase. Images processed using the PSF for $d_o = 146.5''$ at (a) 180", (b) 146.5" and (c) 113". (d)-(f) Images processed using the PSF for $d_o = 180''$.

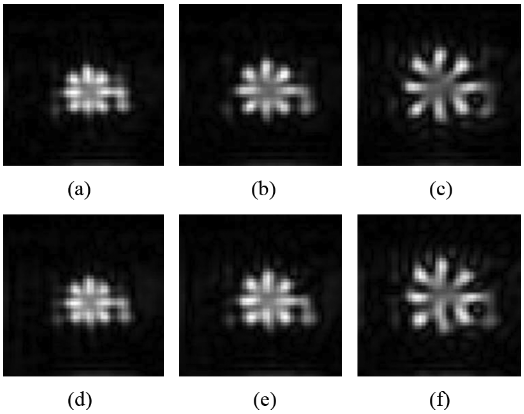

Fig. 12. Processed images from a system with cubic phase. Images processed using the PSF for $d_o = 146.5''$ at (a) 180", (b) 146.5" and (c) 113". (d)-(f) Images processed using the PSF for $d_o = 180''$.

the cubic OTF was estimated from the experiment PSF at 180". From Fig. 4, data collected at 113" has significant high frequency loss in comparison to that collected at both 146.5" and 180". We, therefore, did not use this data to create a reconstruction filter.

In both instances the best reconstruction occurs for the image matched to the filter and the noisest reconstruction is at 113", which one would expect. Nonetheless, the reconstructions of the point response are comparable in terms of spatial scale to the in-focus response of the conventional system. Compare Fig. 11(a), (b), (d), and (e) to Fig. 8(a). Thus, we have extended the region over which the system generates a diffraction-limited spot from 5" in front of the focal plane to 34". Since we expect similar behavior for objects beyond the focal plane, the depth of field has been expanded in that direction by at least 34" as well but we expect considerably more.

This behavior is reflected also in the reconstruction of the extended object represented in Fig. 12. For both reconstructions, not only are the images at 180" comparable to the focused image from the conventional system but the images at 146.5" are comparable as well. In comparison to the image at 146.5" from the conventional system, the reconstructed images display higher contrast and higher resolution. Note especially the reflection off the metal plate on the right-hand side, which is clearly visible in the reconstructions but is apparent only in the focused conventional image in Fig. 10.

VI. SUMMARY

We applied a computational imaging technique for extending depth-of-field at optical frequencies to a millimeter wave imaging system. The technique requires inserting a cubic phase element in the pupil plane of an imaging system and subsequent post-detection signal processing. We designed and fabricated the cubic phase element in Rexolite and validated its performance experimentally.

In some applications, *a priori* range information can be used to improve estimated PSFs and thereby improve restoration. Further, non-linear image restoration techniques incorporating *a priori* knowledge of the scene can improve restoration relative to linear restoration.

A critical difference between the performance of millimeter wave imaging systems and imaging systems for optical and infrared wavelengths is the underlying phenomonology and availability of technology, especially detector arrays. Millimeter wave systems image temperature contrasts. Careful analysis of noise and contrast in such systems is necessary to assess the impact of inserting an element into the optical train whose amplitude transfer function, although flat, is relatively low. A more in-depth analysis should also consider the coherence and spectral bandwidth of the illumination.

In addition, in terms of practical application, one needs to consider the scale of the optical system and the lack of large arrays of millimeter wave detectors on system design. Whereas one can design an optical staring imager, millimeter wave systems will continue to be scanning systems until detector array technology matures. Even so, given the physical constraint on the security system mentioned in the introduction, it is unlikely that a such system will have a detector array larger than 200 × 200. Nonetheless, the applicability and advantage of computational imaging techniques to millimeter wave systems has been demonstrated.

REFERENCES

[1] A. Luukanen, A. J. Miller, and E. N. Grossman, "Passive hyperspectral terahertz imagery for security screening using a cryogenic microbolometer, Passive millimeter-wave imaging technology VIII," in *Proc. SPIE*, R. Appleby and D. A. Wikner, Eds. Bellingham, WA: SPIE, 2005, vol. 5789, pp. 127–134.

[2] L. Yujiri, M. Shoucri, and P. Moffa, "Passive millimeter-wave imaging," *IEEE Microw. Mag.*, vol. 4, pp. 39–50, Sep. 2003.

[3] R. Appleby and H. B. Wallace, "Standoff detection of weapons and contraband in the 100 GHz to 1 THz region," *IEEE Trans. Antennas Propag.*, vol. 55, pp. 2944–2956, Nov. 2007.

[4] E. R. Dowski , Jr and W. T. Cathey, "Extended depth of field through wave-front coding," *Appl. Opt.*, vol. 34, pp. 1859–1866, 1995.

[5] J. van der Gracht, E. R. Dowski, W. T. Cathey, and J. Bowen, "Aspheric optical elements for extended depth of field, novel optical system design and optimization," in *SPIE Proc.*, J. M. Sasian, Ed. Bellingham, WA: SPIE, 1995, vol. 2537, pp. 279–288.

[6] J. van der Gracht, E. R. Dowski , Jr, M. G. Taylor, and D. M. Deaver, "Broadband behavior of an optical-digital focus-invariant system," *Opt. Lett.*, vol. 21, pp. 919–921, 1996.

[7] S. Bradburn, W. T. Cathey, and E. R. Dowski, "Realizations of focus invariance in optical-digital systems with wave-front coding," *Appl. Opt.*, vol. 36, pp. 9157–9166, 1997.

[8] W. T. Cathey and E. R. Dowski, "New paradigm for imaging systems," *Appl. Opt.*, vol. 41, pp. 6080–6092, 2002.

[9] R. Athale, D. M. Healy, D. J. Brady, and M. A. Neifeld, "Reinventing the camera," *Opt. Photon. News*, vol. 19, no. 3, pp. 32–37, Mar. 2008.

[10] D. A. Wikner and G. Samples, "Polarimetric passive millimeter-wave sensing, passive millimeter-wave imaging technology V," in *SPIE Proc.*, R. M. Smith and R. Appleby, Eds. Bellingham, WA: SPIE, 2001, vol. 4373, pp. 86–93.

[11] J. W. Goodman, *Introduction to Fourier Optics*, 3rd ed. Englewood, CO: Roberts and Company, 2005.

[12] F. L. Pedrotti and L. S. Pedrotti, *Introduction to Optics*. Englewood Cliffs, NJ: Prentice-Hall, 1987, p. 125.

[13] C. L. Fales, F. O. Huck, and R. W. Samms, "Imaging system design for improved information capacity," *Appl. Opt.*, vol. 23, pp. 872–888, 1984.

Joseph N. Mait (S'78–M'84–SM'03) received the B.S.E.E. degree from the University of Virginia, Charlottesville, in 1979 and the M.S.E.E. and Ph.D. degrees from the Georgia Institute of Technology, Atlanta, in 1980 and 1985, respectively.

Since 1989, he has been with the U.S. Army Research Laboratory, Adelphi, MD, where he is currently Senior Technical Researcher (ST) for Electromagnetics. He was an Assistant Professor of electrical engineering at the University of Virginia from 1984 to 1989 and an Adjunct Associate Professor at the University of Maryland, College Park, from 1997 to 2005. He has also held visiting positions at the Lehrstuhl für Angewandte Optik, Universität Erlangen-Nürnberg, Germany, and the Center for Technology and National Security Policy, National Defense University, Washington, DC. His research interests include the application of optics, photonics, and electromagnetics to sensing and sensor signal processing.

Dr. Mait is a Fellow of SPIE and OSA.

David A. Wikner received the B.A. degree in physics from Ohio Wesleyan University, Delaware, in 1986 and the M.S. degree in physics from Stanford University, Palo Alto, CA, in 1988.

Currently, he leads the Millimeter Wave Phenomenology Team, Army Research Laboratory, Adelphi, MD. He is responsible for the exploration of MMW imaging techniques and signature analysis, system design, and new device technology. He has worked extensively with 94-GHz radar systems for vehicle and ground clutter measurements. He has also designed and built a W-band Stokes-vector radiometer for fundamental phenomenology measurements. He has published 20 papers on the subject of MMW phenomenology and technology. In the last several years, his work has focused on efforts to create affordable MMW imaging systems for U.S. Army applications and techniques for creating enhanced imaging through computational optics.

Mark S. Mirotznik (S'87–M'92) received the B.S.E.E. degree from Bradley University, Peoria, IL, in 1988 and the M.S.E.E. and Ph.D. degrees from the University of Pennsylvania, Philadelphia, in 1991 and 1992, respectively.

Since 1992, he has been a faculty member in the Department of Electrical Engineering, The Catholic University of America, Washington, DC, where, in 1997, he was promoted to Associate Professor. He also holds the position of Senior Research Engineer for the Naval Surface Warfare Center (NSWC), Carderock Division. His research interests include applied electromagnetics and photonics, computational electromagnetics and bioelectromagnetics.

Joseph van der Gracht received the Ph.D. degree in electrical engineering with an emphasis in modern optics from the Georgia Institute of Technology, Atlanta, in 1991.

Since beginning his professional career in 1979, he has worked for Texas Instruments, Mead and Rockwell International on a variety of optoelectronics related technologies. In 1991, he was a Principal Investigator at the U.S. Army Research Laboratory, Adelphi, MD. He is currently a Senior Engineer at HoloSpex, Inc., Columbia, MD, responsible for digital holography and imaging. His main research efforts are directed toward investigating new imaging modalities that optimize the information content of a scene through the use of novel optical elements, unorthodox detector geometries and post-detection signal processing.

Gregory P. Behrmann received the B.S.M.E. degree from Drexel University, Philadelphia, PA and the M.S.M.E. degree from The Johns Hopkins University, Baltimore, MD. He is currently working toward the Ph.D. degree at the Catholic University of America, Washington, DC.

Previously, he has held senior engineering positions at the U.S. Army Research Laboratory, Potomac Photonics, Inc., and Corvis Corporation.

Brandon L. Good is currently working toward the M.S. degree at the Catholic University of America, Washington, DC.

Scott A. Mathews (M'06) received the B.S. degree in physics, the M.S. degree in materials engineering, and the Ph.D. degree in materials engineering from the University of Maryland, College Park, in 1988, 1993, and 2001, respectively.

In 2003, he joined the Electrical Engineering Department, Catholic University of America, Washington, DC, where he is an Assistant Professor. Prior to joining Catholic University, he did research and development in the private sector for 15 years, including work on solid state radiation imaging systems, optical data storage systems, and laser micro-fabrication of microelectronic and microfluidic structures. He is interested in miniature, electronic detection systems for chemical and biological warfare agents.